Submitted to *Chem. Commun.*, 2017

SUPPORTING INFORMATION

An Organolanthanide(III) Single-Molecule Magnet with an Axial Crystal-Field: Influence of the Raman Process Over the Slow Relaxation.

Jérôme Long,*[a] Boris G. Shestakov,[b] Dan Liu,[c] Liviu F. Chibotaru,[c] Yannick Guari [a], Anton V. Cherkasov,[b] Georgy K. Fukin,[b] Alexander A. Trifonov,*[b,d] and Joulia Larionova. [a]

[a] Institut Charles Gerhardt Montpellier, UMR 5253, Ingénierie Moléculaire et Nano-Objets, Université de Montpellier , ENSCM, CNRS, place E. Bataillon, 34095 Montpellier Cedex 5 (France). E-mail: jerome.long@umontpellier.fr

[b] Institute of Organometallic Chemistry of Russian Academy of Scienes, Tropinina 49, GSP-445, 630950, Nizhny Novgorod Russia.

[c] Theory of Nanomaterials Group and INPAC, Katholieke Universiteit Leuven, Celesijnenlaan, 200F, Heverlee, B-3001, Belgium.

[d] Institute of Organoelement compounds of Russian Academy of Sciences, Vavilova str. 28, 119334, Moscow, Russia. E-mail: trif@oimc.ras.ru

Experimental

Synthesis

General Remarks. All procedures were performed under vacuum using standard Schlenk and glove-box techniques. After drying over KOH, THF and DME were distilled from sodium benzophenone ketyl prior to use. Hexane and toluene were purified by distillation from sodium/triglyme benzophenone ketyl or CaH_2. 2,6-$iPr_2C_6H_3N$=CH-CH=$NC_6H_3Pri_2$-2,6,[1] anhydrous $LnCl_3$ were obtained following the published synthetic procedures.[2] All other commercially available chemicals were used after the appropriate purification. IR spectra were recorded on Bruker-Vertex 70 instrument as Nujol mulls. The UV-VIS spectra were recorded in evacuated quartz cuvettes on a Perkin-Elmer Lambda 25 spectrophotometer. Lanthanide metal analyses were carried out by complexometric titration.[3] Elemental analyses were performed by the Microanalytical laboratory of the Institute of Organometallic Chemistry of RAS.

Synthesis of [Li(DME)$_3$][(2,6-*i*Pr$_2$C$_6$H$_3$NCHCHNC$_6$H$_3$*i*Pr$_2$-2,6)$_2$Dy] (1a). A THF (20 mL) solution of [2,6-*i*Pr$_2$C$_6$H$_3$NCHCHNC$_6$H$_3$*i*Pr$_2$-2,6]Li$_2$(THF)$_n$ obtained *in situ* from 2,6-*i*Pr$_2$C$_6$H$_3$NCHCHNC$_6$H$_3$*i*Pr$_2$-2,6 (0.810 g, 2.15 mmol) and Li (0.030 g, 4.30 mmol) was slowly added to a suspension of $DyCl_3$ (0.290 g, 1.08 mmol) in THF (5 mL) at room temperature and the reaction mixture was stirred for 10 h. The volatiles were evaporated and the solid residue was extracted with toluene (15 mL). The toluene extract was filtered, toluene was removed in vacuum. Recrystallization of the resulting solid from DME at –20 °C afforded yellow crystals of 1 (0.530 g, 40% yield). IR (KBr, Nujol): ν = 1620 (w), 1593 (m), 1540 (m), 1315 (m), 1257 (s), 1183 (w), 1101 (w), 1053 (s), 929 (w), 857 (m), 796 (m), 756 (m) cm^{-1}; elemental analysis calcd. (%) for $C_{65.89}H_{106.71}DyLiN_4O_{6.94}$ (1235.40 g·mol^{-1}): C, 64.06; H, 8.70; N, 4.54; Dy, 13.15; found: C, 63.75; H, 8.47; N, 4.52; Dy, 12.90.
Recrystallization of the crude product from DME-hexane mixture at room temperature afforded **1b** in 63 %. Elemental analysis calcd. (%) for $C_{68.5}H_{112.5}DyLiN_4O_6$ (1257.56): C, 65.42; H, 9.01; N, 4.45; Dy, 12.92; found: C, 65.79; H, 8.72; N, 4.13; Dy, 12.77.

Synthesis of [Li(DME)$_3$][(2,6-*i*Pr$_2$C$_6$H$_3$NCHCHNC$_6$H$_3$*i*Pr$_2$-2,6)$_2$Tb] (2). A THF (20 mL) solution of [2,6-*i*Pr$_2$C$_6$H$_3$NCHCHNC$_6$H$_3$*i*Pr$_2$-2,6]Li$_2$(THF)$_n$ obtained *in situ* from 2,6-*i*Pr$_2$C$_6$H$_3$NCHCHNC$_6$H$_3$*i*Pr$_2$-2,6 (0.500 g, 1.33 mmol) and Li (0.019 g, 2.66 mmol) was slowly added to a suspension of $TbCl_3$ 0.17 g (0.64 mmol) in THF (15 mL) at room temperature and the reaction mixture was stirred for 48 h. The resulting dark-red solution was filtered, the solvent was evaporated in vacuum and the resulting solid residue was extracted with toluene (20 mL). The extracts were filtered, toluene was then evaporated in vacuum and the remaining solid was redissolved in DME (~2 mL). Slow condensation of hexane into the DME solution at 20 °C afforded yellow crystals of 1 (0.51 g, 60%). IR (Nujol, KBr, cm^{-1}): 1628(w), 1588 (s), 1563 (m), 1325 (m), 1255 (m), 1113 (s), 1088 (s), 981 (m), 926 (m), 855 (m), 799 (s), 752 (m), 696 (m), 553 (m). Anal. Calcd for $C_{69}H_{114}LiN_4O_7Tb$ (1277.50): C, 64.87; H, 8.99; N, 4.38; Tb, 12.43; found: C, 64.59; H, 8.79; N, 3.99; Tb 12.63.

Synthesis of [Li(DME)$_3$][(2,6-*i*Pr$_2$C$_6$H$_3$NCHCHNC$_6$H$_3$*i*Pr$_2$-2,6)$_2$Er] (3). A THF (20 mL) solution of [2,6-*i*Pr$_2$C$_6$H$_3$NCHCHNC$_6$H$_3$*i*Pr$_2$-2,6]Li$_2$(THF)$_n$ obtained *in situ* from 2,6-*i*Pr$_2$C$_6$H$_3$NCHCHNC$_6$H$_3$*i*Pr$_2$-2,6 (0.700 g, 1.86 mmol) and Li (0.026 g, 3.72 mmol) was slowly

added to a suspension of $ErCl_3$ (0.250 g, 0.91 mmol) in THF (15mL) at room temperature and the reaction mixture was stirred for 48 h. The resulting dark-red solution was filtered, the solvent was evaporated in vacuum, the remaining solid residue was extracted with toluene (25 mL) and the extracts were filtered. After evaporation of toluene in vacuum the solid was dissolved in DME (~2 mL). Slow diffusion of hexane into the DME solution at 20 °C afforded orange crystals of 2 (0.67 g, 58%). IR (Nujol, KBr, cm^{-1}): 1627(w), 1588 (s), 1261 (s), 1210 (w), 1118 (m), 1032 (s), 1006 (w), 925 (m), 860 (m), 794 (m), 755 (m), 698 (m), 551 (w). Anal. Calcd for $C_{67}H_{109}ErLiN_4O_6$ (1240.78): C, 64.85; H, 8.85; N, 4.51; Er, 13.48; found: C, 64.66; H, 8.69; N, 4.32; Er, 13.83.

Single-Crystal X-ray Diffraction. The X-ray data for **1**–**3** was collected on *Bruker D8 Quest* (**1b, 2**), *Agilent Xcalibur E* (**1a**, **3**) diffractometers (MoK_α radiation, ω-scans technique, $\lambda = 0.71073$ Å, $T = 100(2)$ K). The structures **1**–**3** were solved by direct and dual-space methods[4] and were refined by full-matrix least squares on F^2 for all data using *SHELX*.[5] *CrysAlis PRO*[6] and *SADABS*[7] were used to perform area-detector scaling and absorption corrections. All non-hydrogen atoms were found from Fourier syntheses of electron density and were refined anisotropically. All hydrogen atoms were placed in calculated positions and were refined in the "riding" model with $U_{iso}(H) = 1.2U_{eq}$ of their parent atoms ($U_{iso}(H) = 1.5U_{eq}$ for CH_3-groups). Two ^iPr-groups in **2**, all 2,6-$^iPr_2C_6H_3$-fragments of anionic part $[Dy(DAD)_2]^-$ in **1a**, one ^iPr-group in **1b**, all DME molecules of cationic part $[Li(DME)_3]^+$ in **2** and **1a** disordered over two sites. Displacement parameters of equivalent atoms of disordered fragments were restrained with *RIGU*, *EADP* and *ISOR* instructions; bond distances in disordered fragments were restrained with *DFIX* and *SADI* instructions.

CCDC-1461678 (**1a**), 1476447 (**1b**), 1476449 (**2**), 1476448 (**3**), contain the supplementary crystallographic data for this paper. These data are provided free of charge by The Cambridge Crystallographic Data Centre.

Magnetic Measurements

Magnetic susceptibility data were collected with a Quantum Design MPMS-XL SQUID magnetometer working between 1.8 – 350 K with the magnetic field up to 7 Tesla. The sample was prepared in a glove box. The data were corrected for the sample holder and the diamagnetic contributions calculated from the Pascal's constants.

Computational Details.

All calculations were carried out with MOLCAS 8.0 and are of CASSCF/RASSI/SINGLE_ANISO type. Structures of **1**a, **2** and **3** and are shown below.

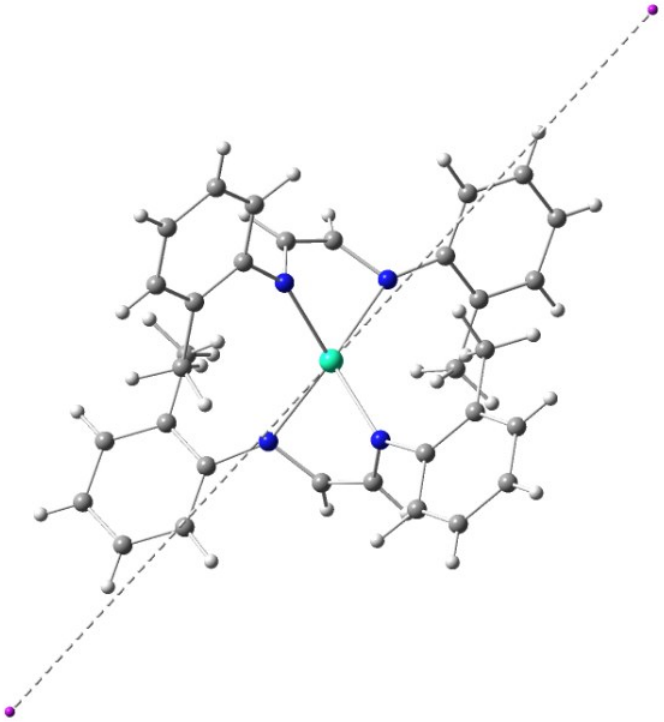

Structure of the $Li(DME)_3[Dy(DAD)_2]$ complex **1a**. The dashed line shows the main anisotropy axis of the ground state.

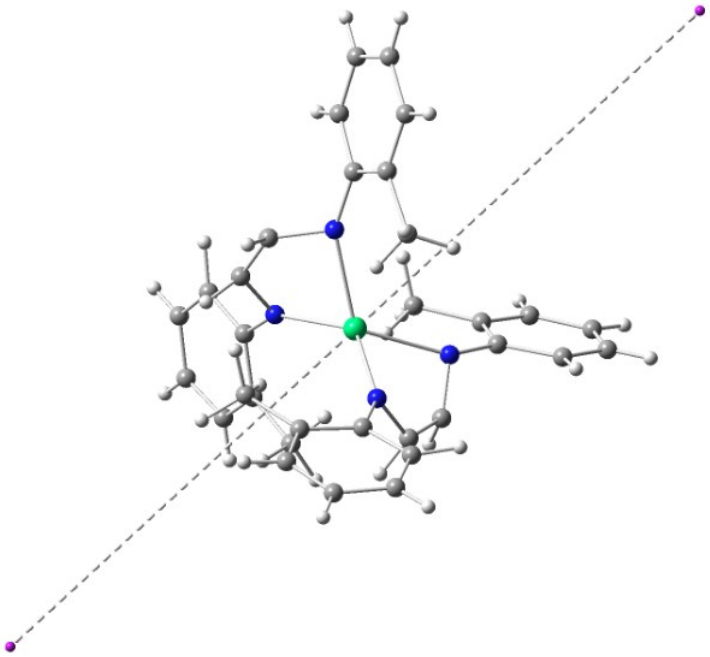

Structure of the $Li(DME)_3[Er(DAD)_2]$ complex **3**. The dashed line shows the main anisotropy axis of the ground state.

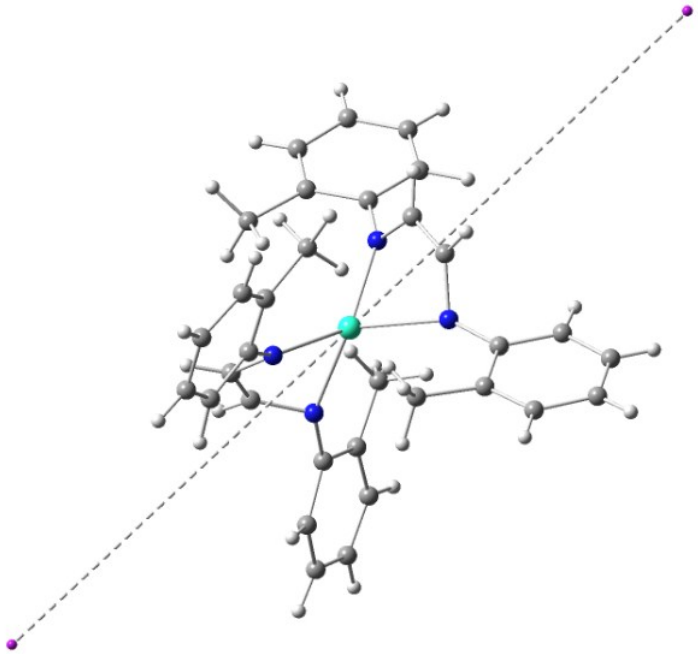

Structure of the $Li(DME)_3[Tb(DAD)_2]$ complex **2** complex. The dashed line shows the main anisotropy axis of the ground state.

The Dy, Er and Tb centers were calculated omitting atoms far away from the center and using the experimentally determined coordinates of atoms.

Two basis set approximations have been employed: **1** Basis– small, and **2** Basis– large. Tables 1-4 show the contractions of the employed basis sets for all elements for **1** - **3**.

Contractions of the employed basis sets in computational approximations for compound **1**.

Basis 1	**Basis 2**
DY.ANO-RCC...7S6P4D2F1G.	DY.ANO-RCC...8S7P5D3F2G1H.
N.ANO-RCC...3S2P.	N.ANO-RCC...3S2P1D.
C.ANO-RCC...3S2P.	C.ANO-RCC...3S2P.
H.ANO-RCC...2S.	H.ANO-RCC...2S.

Contractions of the employed basis sets in computational approximations for **3**.

Basis 1	**Basis 2**
ER.ANO-RCC...7S6P4D2F1G.	ER.ANO-RCC...8S7P5D3F2G1H.
N.ANO-RCC...3S2P.	N.ANO-RCC...3S2P1D.
C.ANO-RCC...3S2P.	C.ANO-RCC...3S2P.
H.ANO-RCC...2S.	H.ANO-RCC...2S.

Contractions of the employed basis sets in computational approximations for **2**.

Basis 1	**Basis 2**
TB.ANO-RCC...7S6P4D2F1G.	TB.ANO-RCC...8S7P5D3F2G1H.
N.ANO-RCC...3S2P.	N.ANO-RCC...3S2P1D.
C.ANO-RCC...3S2P.	C.ANO-RCC...3S2P.

H.ANO-RCC...2S.	H.ANO-RCC...2S.

Active space of the CASSCF method included 9 electrons in 7 orbitals for the Dy center (4*f* orbitals of Dy^{3+} ion), 8 electrons in 7 orbitals for the Tb center (4*f* orbitals of Tb^{3+} ion), 11 electrons in 7 orbitals for the Er center (4*f* orbitals of Er^{3+} ion).

Considering the spin-orbit coupling, for the Dy center, the CASSCF calculation is executed at ground state(S=6) with all of the 21 configurations, the first excited state(S=4) with all of the 224 configurations and the second excited state(S=2) with all the 490 configurations. After the CASSCF calculation, the RASSI calculation of RAS state interaction is performed 21 configurations for the ground state(S=6); 128 configurations for the state (S=4) and 130 configurations for the state (S=2). For the Er center, both the CASSCF and RAS calculation are executed at the ground state (S=4) with all of the 35 configurations, the state S=2 with all of the 112 configurations. For the Tb center, the CASSCF calculation is executed at ground state (S=7) with all of 7 configurations, the first excited state (S=5) with all of the 140 configurations, the second excited state (S=3) with all of 588 configurations and the third excited state (S=1) with all of 490 configurations. The RASST calculation of RAS state interaction is performed 7 configurations for the ground state (S=7), 140 configurations for the first excited state (S=5), 113 configurations for the second excited state (S=3) and 123 configurations for the third excited state (S=1).

On the basis of the resulting spin-orbital multiplets SINGLE_ANISO program computed local magnetic properties (*g*-tensors, magnetic axes, local magnetic susceptibility, etc.)

Magnetic Properties

DC magnetic properties of 1a.

It has been noticed that the number of solvates DME molecules in **1a** may vary. The magnetic results have been obtained considering the presence of two solvates molecules. The temperature dependence of the magnetic susceptibility performed with an applied magnetic field of 1000 Oe for 1a reveals that the room temperature χT value is equal to 14.05 $cm^3.K.mol^{-1}$, which is close to the theoretical value of 14.17 $cm^3.K.mol^{-1}$ expected for one Dy^{3+} ion ($^6H_{15/2}$, S = 5/2, L = 5) (Fig. S2). Upon cooling, a decrease of χT occurs due to the thermal depopulation of the Stark sub-levels to reach the value of 10.05 $cm^3.K.mol^{-1}$ at 1.8 K. The field dependence of the magnetization at 1.8 K reaches the values of 5.26 μB at 7 T (Inset of Fig. S2) without a clear saturation.

DC magnetic properties of 1b.

The temperature dependence of the magnetic susceptibility performed with an applied magnetic field of 1000 Oe for **1b** reveals that the room temperature χT value is equal to 14.32 $cm^3.K.mol^{-1}$, which is close to the theoretical value of 14.17 $cm^3.K.mol^{-1}$ expected for one Dy^{3+} ion ($^6H_{15/2}$, S = 5/2, L = 5) (Fig. S2). Upon cooling, a decrease of χT occurs due to the thermal depopulation of the Stark sub-levels to reach the value of 10.66 $cm^3.K.mol^{-1}$ at 1.8 K. The field dependence of the magnetization at 1.8 K reaches the values of 5.26 μB at 7 T (Inset of Fig. S2) without a clear saturation.

Magnetic properties of 2

The magnetic properties of the terbium analogue **2** were investigated. Similarly with Dy^{3+}, the Tb^{3+} ion exhibits an oblate electronic density. However this is a non-Kramers ions ($^7F_6$ ground state). The room temperature value of χT measured for **2** is equal to 11.23 $cm^3.K.mol^{-1}$ which is close to the expected value of 11.82 $cm^3.K.mol^{-1}$ expected for a Tb^{3+} ion considering the free-ion approximation. The observed decrease of χT (Fig. S2) upon cooling is ascribed to the thermal depopulation of the Stark sub-levels. The field dependence of the magnetization at 1.8 K reaches the value of 4.47 μB at 7 T (Inset of Fig. S2) without a clear saturation.

AC measurements were performed in order to check the occurrence of a slow relaxation of the magnetisation. While no significant out-of-phase signal is observed under a zero-dc field, applying weak dc fields induces the appearance of a frequency dependent peaks. The frequency dependence of χ'' at 1.8 K measured for various DC fields leads to the appearance of an out-of-phase component with the highest relaxation time found for a 900 Oe DC field (Fig. S12). A decrease of τ is observed for higher field values, which can be ascribed to the occurrence of the direct relaxation process, which becomes predominant. Taking into account that for this low temperature (1.8 K), the Raman and Orbach processes can be neglected, the field dependence can be reproduced using a simple model recently updated by Zadrozny *et al.* [8] with $\tau^{-1} = DH^2T + B_1/(1+B_2H^2) + K$ (Eq. 3) for which the first term accounts for the direct process (for non-Kramers-ion such as Tb^{3+}), the second one stands for the QTM and the last one is a constant representing the field independent Orbach and Raman process. The obtained parameters are summarized in Table S10. The antagonist effect of the QTM and direct processes gives birth to the maximum observed in the field dependence of τ. The magnitude of

the B_1 and B_2 parameters directly reflects the degree of mixing between the $\pm m_J$ levels and consequently the QTM process.

The frequency dependence at different temperatures under this optimum field of 900 Oe reveals the presence of frequency dependent single peaks (Fig. S13). Their maxima shift to higher temperatures upon increasing frequencies, which clearly indicate a slow relaxation of the magnetisation with out-of-phase signals observed higher than 10 K. The Orbach barrier, estimated from the linear fit, $\tau = \tau_0 \exp(\Delta_{Orbach}/kT)$, gives the parameters $\tau_0 = 6.41 \times 10^{-8}$ s and $\Delta_{Orbach} = 21$ cm^{-1}, confirming a field induced SIM behaviour.

A clear deviation from the linearity appears in the low temperature range (Fig. S14), reflecting the contribution of additional relaxation spin-phonon pathways, such as Raman or direct processes, which show various degree of dependency with temperature. In order to estimate their contribution and extracting a more accurate value of the Δ_{Orbach} barrier, fitting of the temperature dependence of the relaxation time was performed using (Eq. 2) by fixing $m = 7$ (value for non-Kramers ion)[9] and $n = 1$ (usually found for direct process). The best fit gives $\Delta_{Orbach} = 17$ cm^{-1} with $\tau_0 = 2.0 \times 10^{-5}$ s. The non-negligible values of the A and C parameters indicate contributions from both, Raman and direct processes (Table S7). A second method to obtain the value of Δ_{Orbach} was also used: the temperature dependence of the relaxation time was fitted with a model taking into account the influence of the applied magnetic field with the following equation $\tau^{-1} = DH^2T + B_1/(1+B_2H^2) + CT^m + \tau_0^{-1}\exp(-\Delta_{Orbach}/kT)$ (Eq. 4). To avoid over-parameterization, the parameters D, B_1 and B_2 were fixed from the field dependence of the relaxation time. The obtained values of $\Delta_{Orbach} = 12.2$ cm^{-1} and the C parameter (Table S11) are very close to those found with Eq. 2. Cole-Cole plots (Figure S15) and their fitting with a generalized Debye function indicates a very narrow distribution of the relaxation time for the high temperature region ($\alpha = 0.02$), while the value of the α parameter increase to 0.235 upon cooling at 1.8 K, confirming the occurrence of others relaxation processes (Table S12).

Magnetic properties of 3.

In contrast with the Tb^{3+} and Dy^{3+} ions, the Er^{3+} ion exhibits a prolate electronic density. The room temperature value of χT is equal to 11.06 cm^3.K.mol^{-1}, which is close to the expected value of 11.48 cm^3.K.mol^{-1} expected for a Er^{3+} ion considering the free-ion approximation. The observed decrease of χT upon cooling is ascribed to the thermal depopulation of the Stark sub-levels. The field dependence of the magnetization at 1.8 K reaches values of 5.59 μB at 7 T without a clear saturation (Inset of Fig. S2). No out-of-phase signals could be detected at 1.8 K under a zero dc field. Applying weak dc fields shortcut the fast QTM and induces the appearance an out-of-phase susceptibility, but without the presence of a clear maximum (Fig. S17). The temperature dependence of χ'' under a 2500 Oe dc field confirms that the maximum is located lower than 1.8 K (Fig. S18), precluding an in-depth analysis of the relaxation process. Such results confirm that the DAD ligands are particularly adapted to stabilize the electronic density of oblate lanthanide ions.

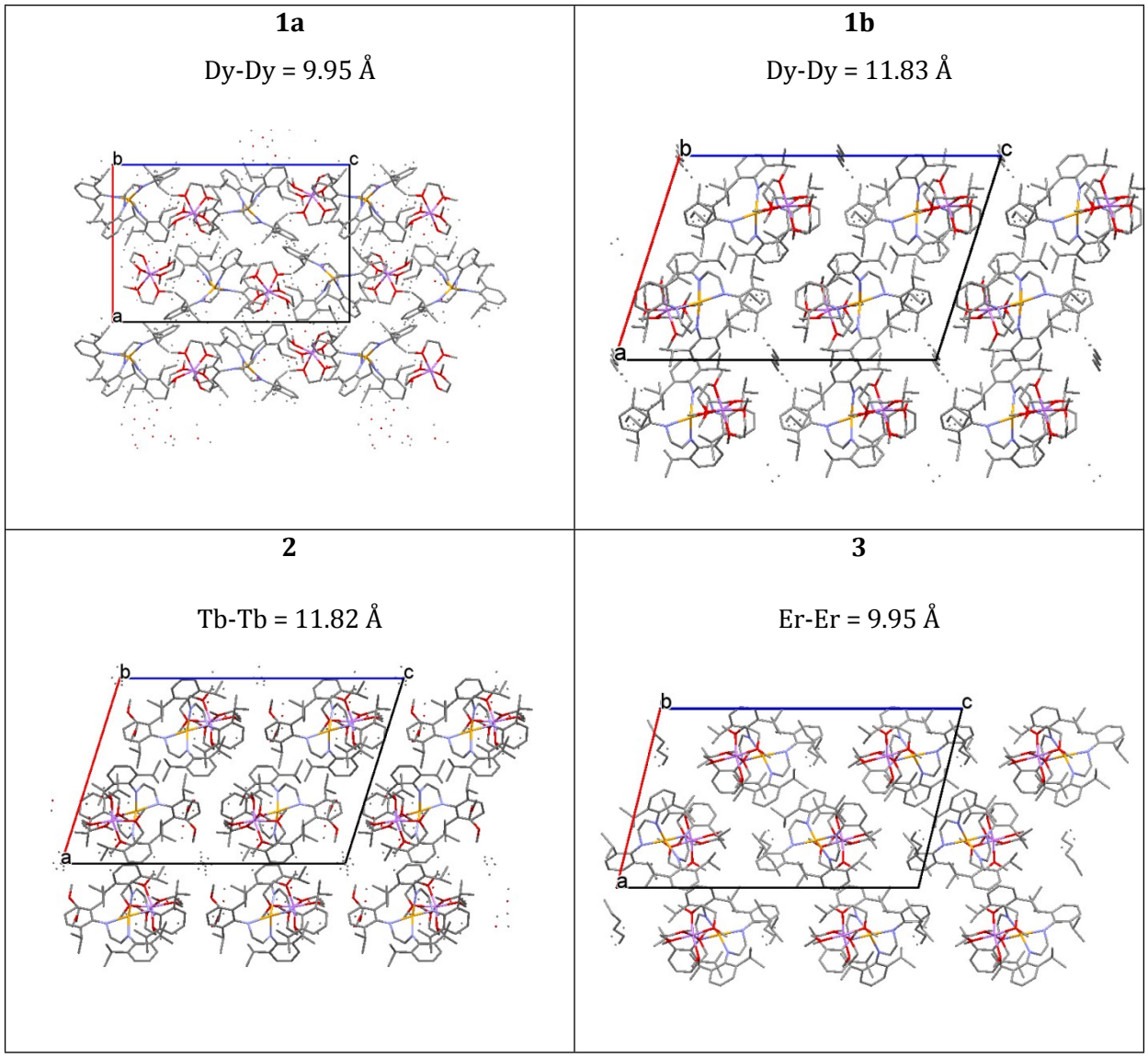

Figure S1. View of the packing arrangement of **1-3** along the *b* crystallographic axis.

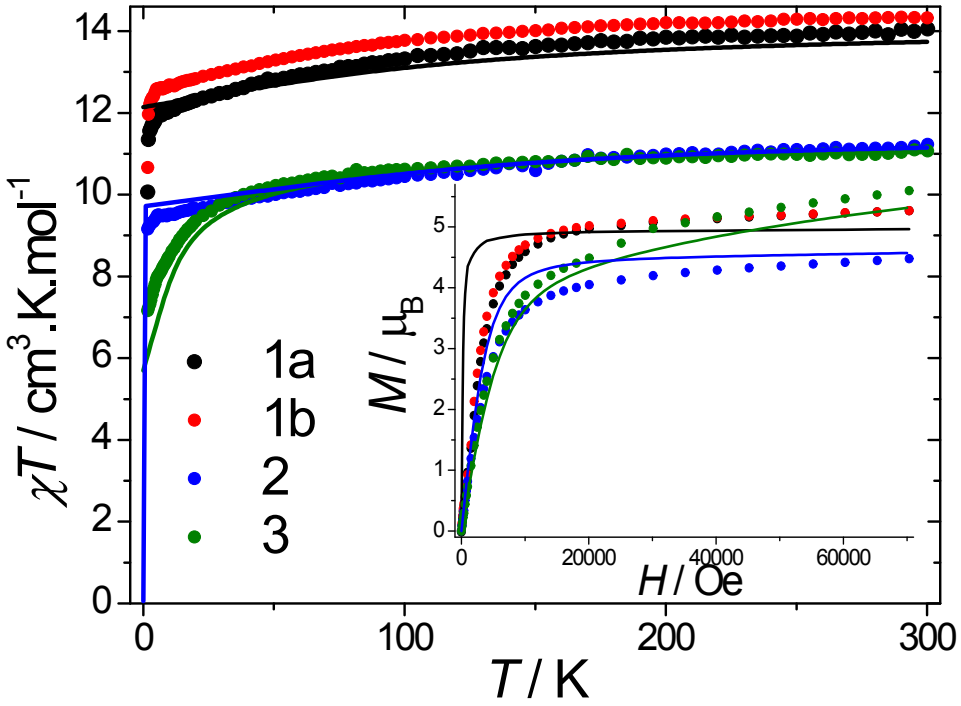

Figure S2. Temperature dependence of χT under a 1000 Oe DC field for **1a**, **1b**, **2**, **3**. The solid lines represent the calculated curves obtained by *ab initio* calculations (dowscaled by 3 and 2% for **2** and **3** respectively). Inset: Field dependence of the magnetisation at 1.8 K. The solid lines represent the calculated curves.

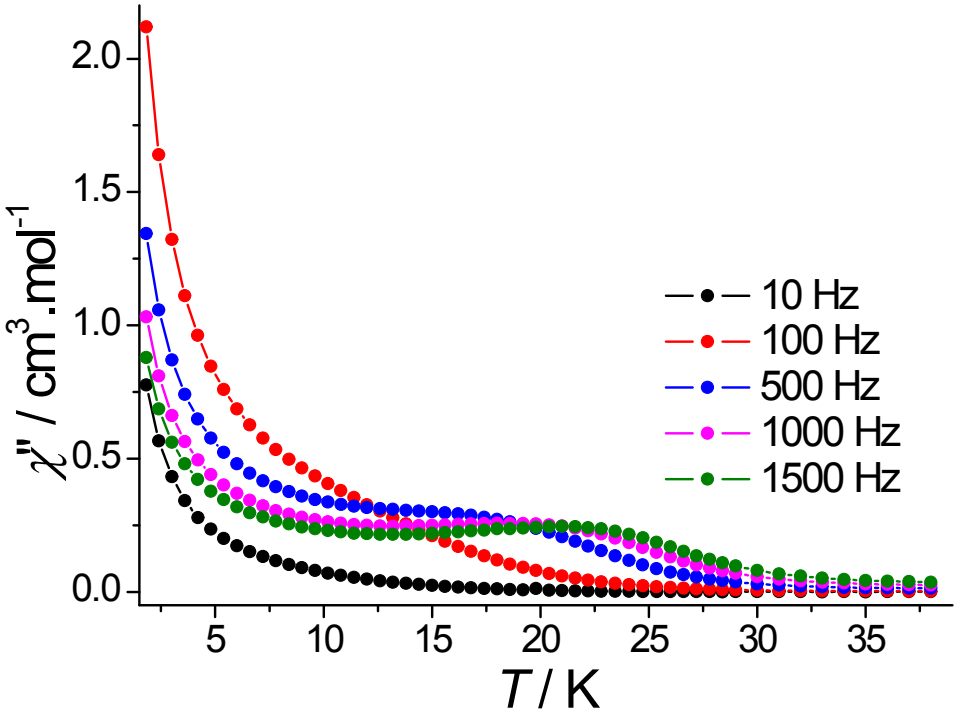

Figure S3. Temperature dependence of the out-of-phase susceptibility, χ'', for different frequencies for **1a**.

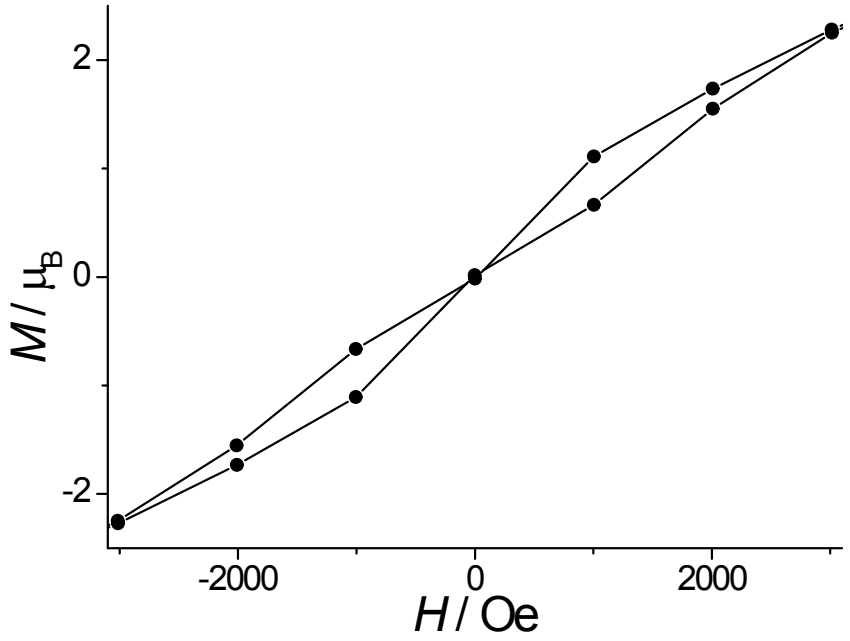

Figure S4. Hysteresis loop for **1a** performed at 1.8 K

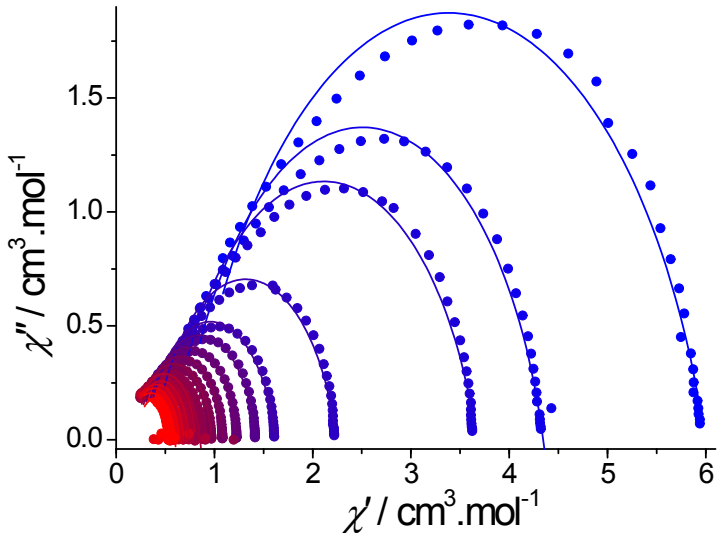

Figure S5. Cole-Cole (Argand) plot obtained using the ac susceptibility data (0 Oe) for **1a**. The solid lines correspond to the best fit obtained with a generalized Debye model.

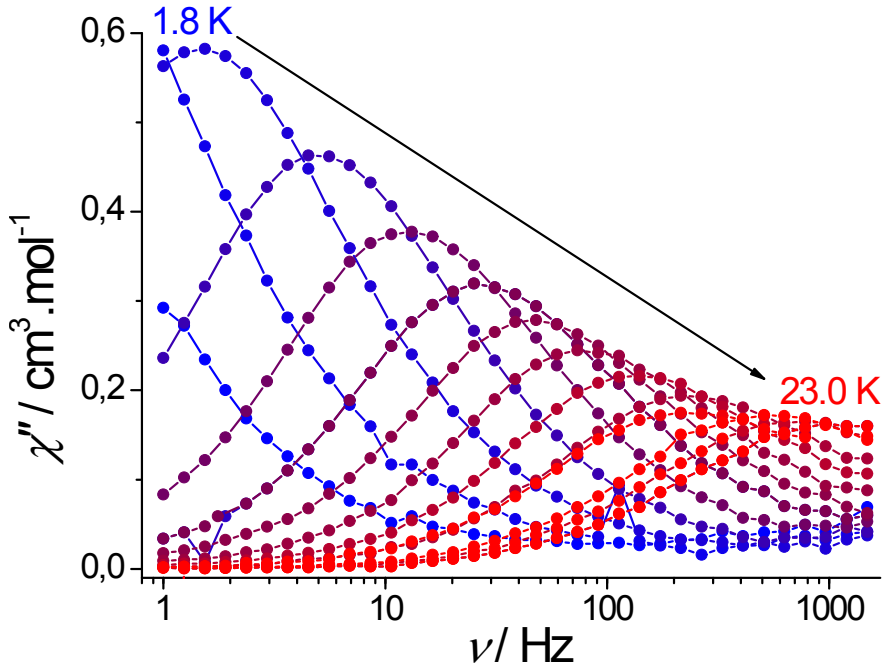

Figure S6. Frequency dependence of the out-of-phase susceptibility, χ'', performed under a 3500 Oe DC field for **1a**.

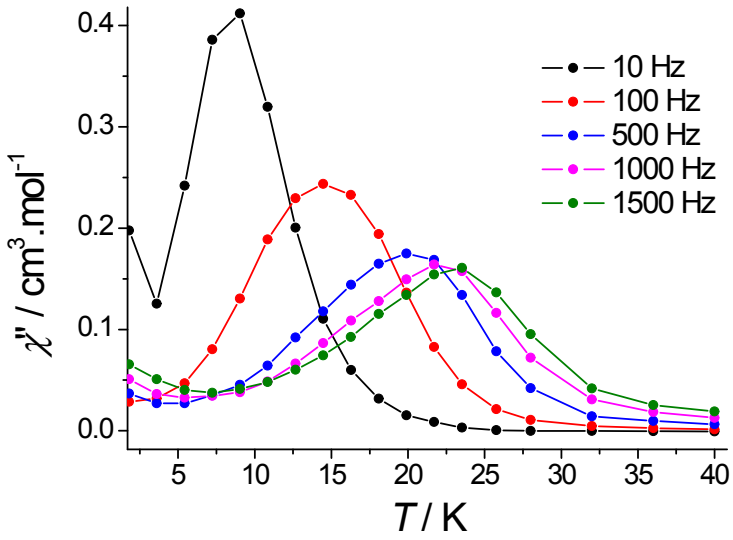

Figure S7. Temperature dependence of the out-of-phase susceptibility, χ'', performed under a 3500 Oe DC field for **1a**.

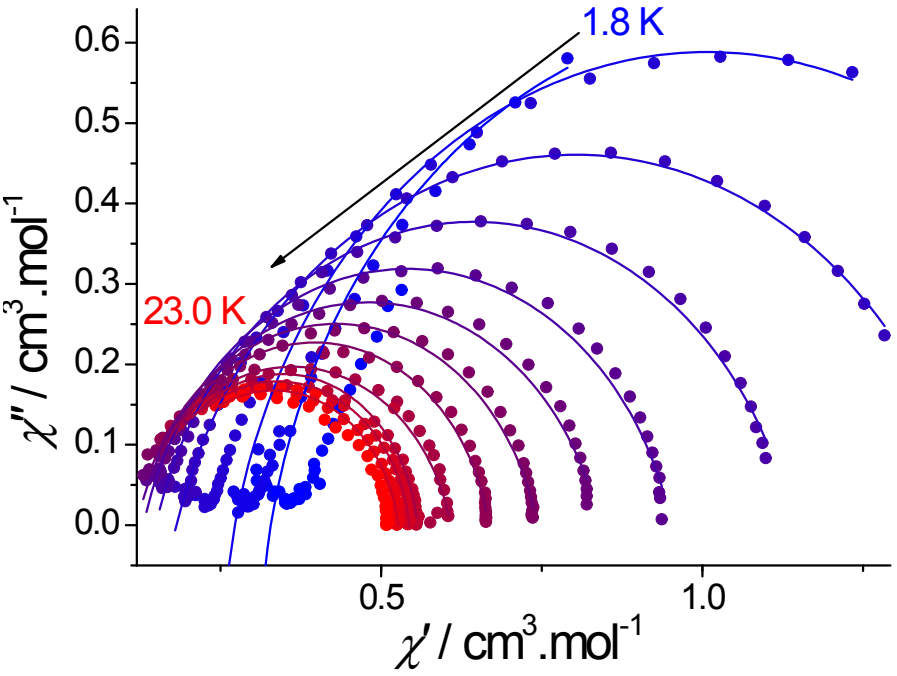

Figure S8 Cole-Cole (Argand) plot obtained using the ac susceptibility data (3500 Oe) for **1a**. The solid lines correspond to the best fit obtained with a generalized Debye model.

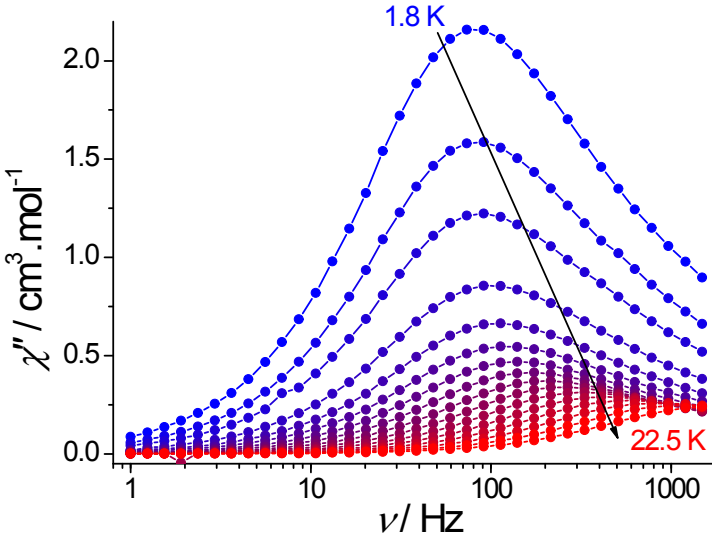

Figure S9. Frequency dependence of the out-of-phase susceptibility, χ'' performed under a zero DC field for **1b**.

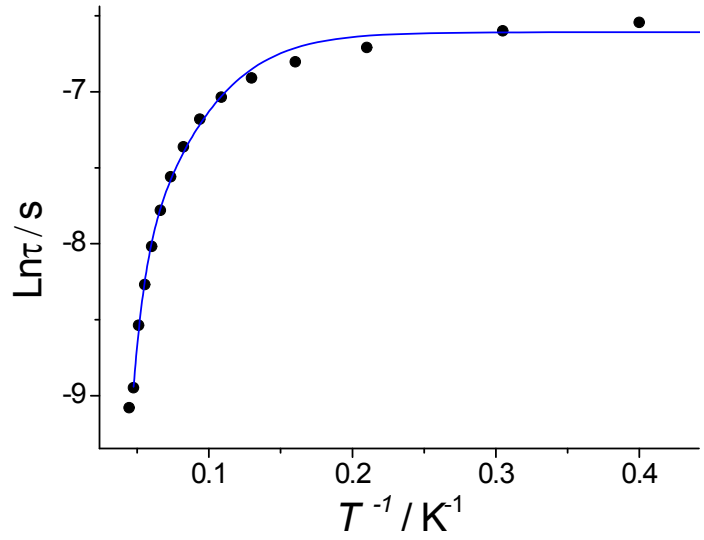

Figure S10. Temperature dependence of the relaxation time K for **1b**. The blue solid line represents the fit using Eq. 2.

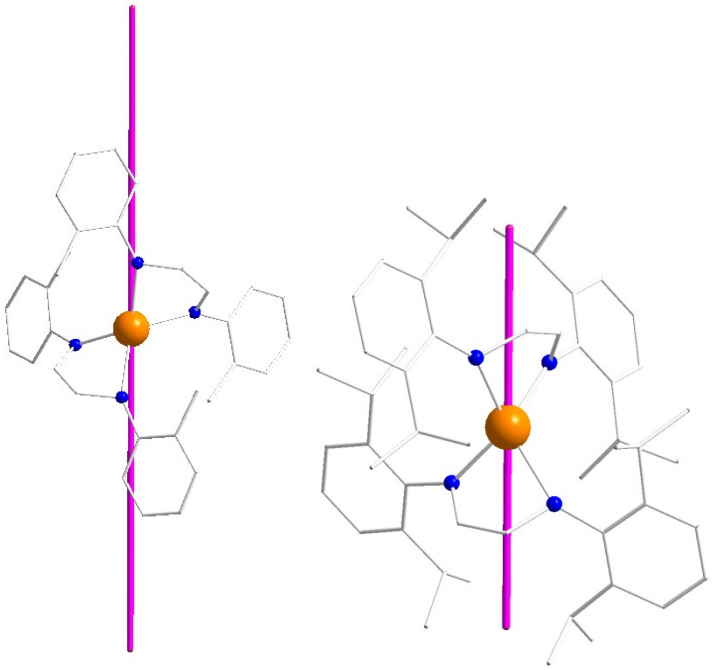

Figure S11. Orientation of the anisotropic axis (purple line) for **1a** obtained from *ab initio* calculations (left) and the MAGELLAN software (right).[10]

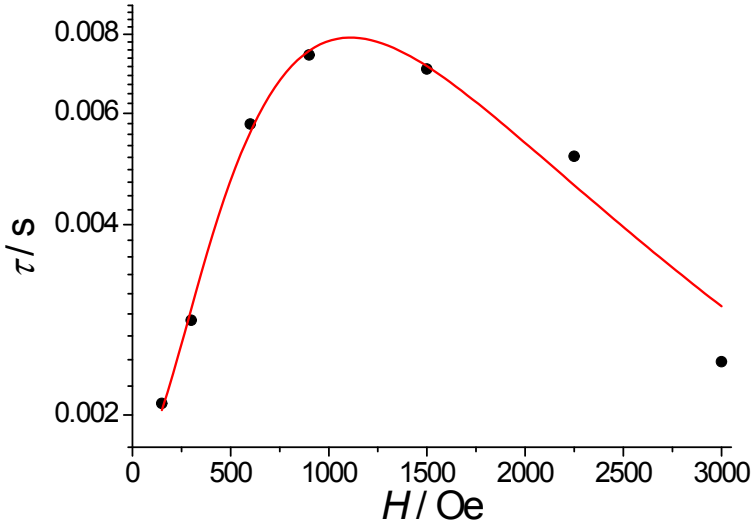

Figure S12. Field dependence of the relaxation time at 1.8 K for **2**. The red solid lines represent the best fit using Eq. 1.

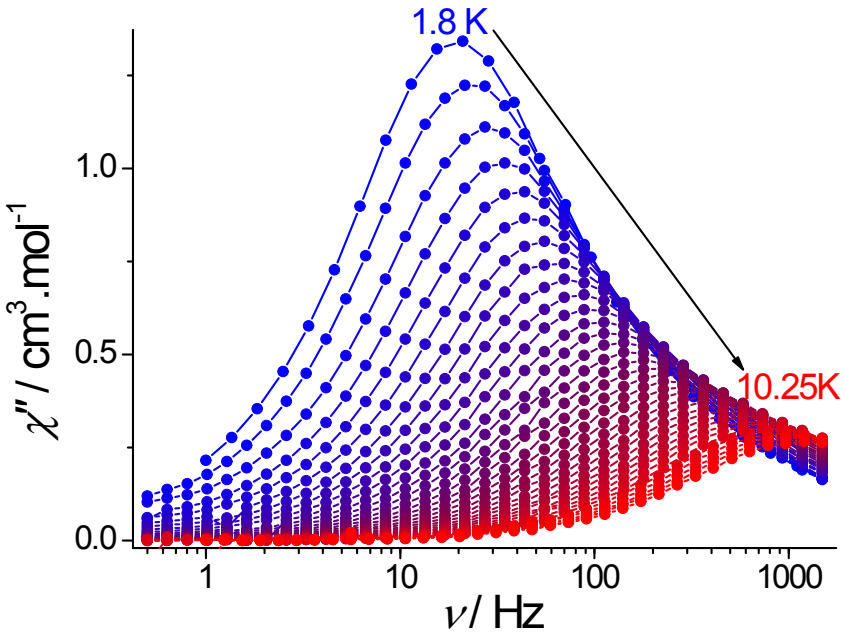

Figure S13. Frequency dependence of the out-of-phase susceptibility, χ'', performed under a 900 Oe DC field for **2**.

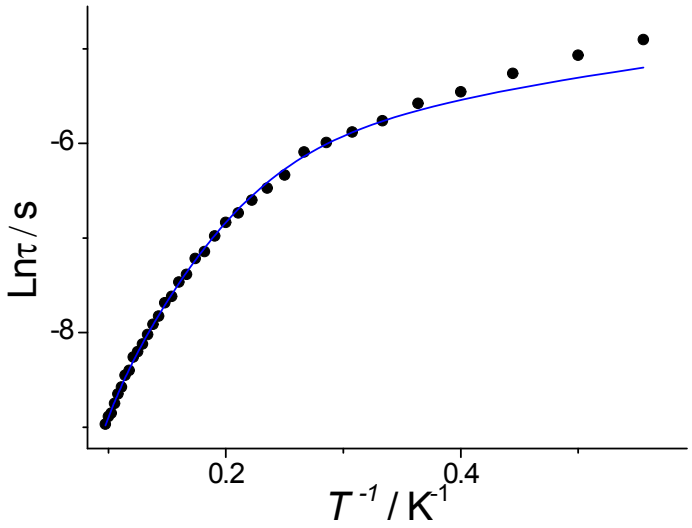

Figure S14. Temperature dependence of the relaxation time for **2**. The blue solid line represents the best fit using Eq. 2.

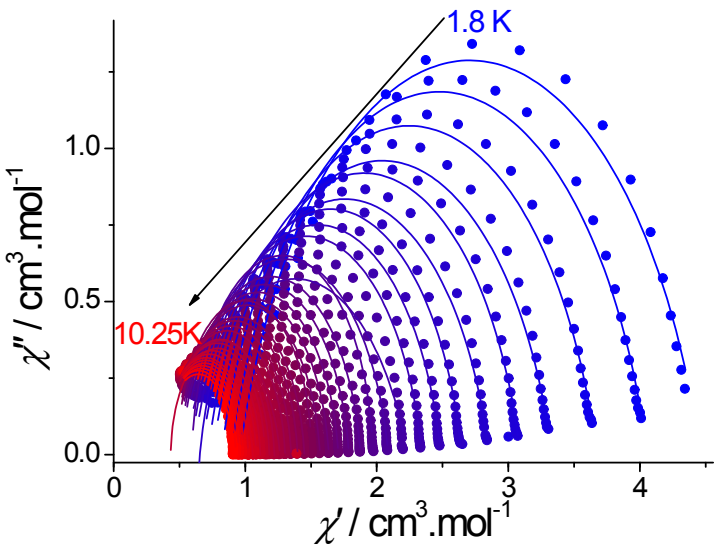

Figure S15. Cole-Cole (Argand) plot obtained using the ac susceptibility data (900 Oe) for **2**. The solid lines correspond to the best fit obtained with a generalized Debye model.

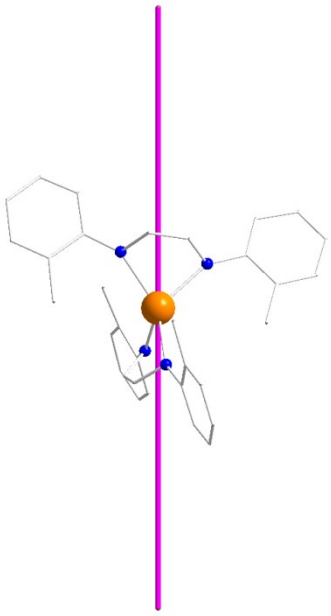

Figure S16. Orientation of the anisotropic axis (purple line) for **2** obtained from *ab initio* calculations.

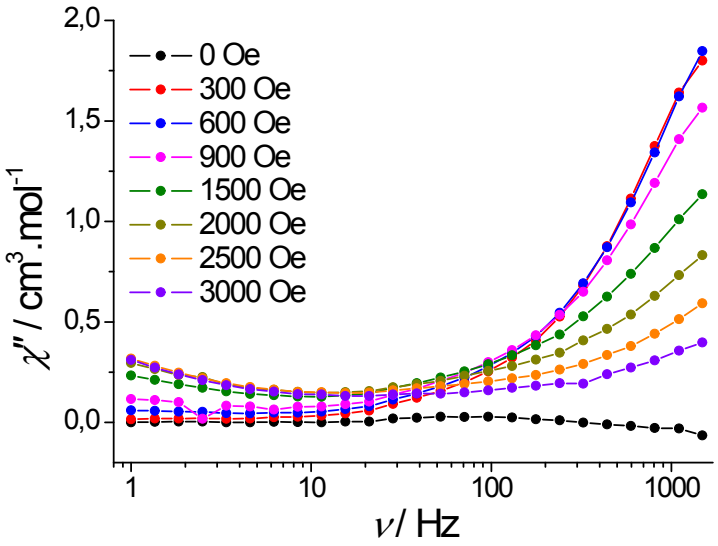

Figure S17 Frequency dependence of the out-of-phase susceptibility, χ'', at 1.8 K for different DC fields for **3**.

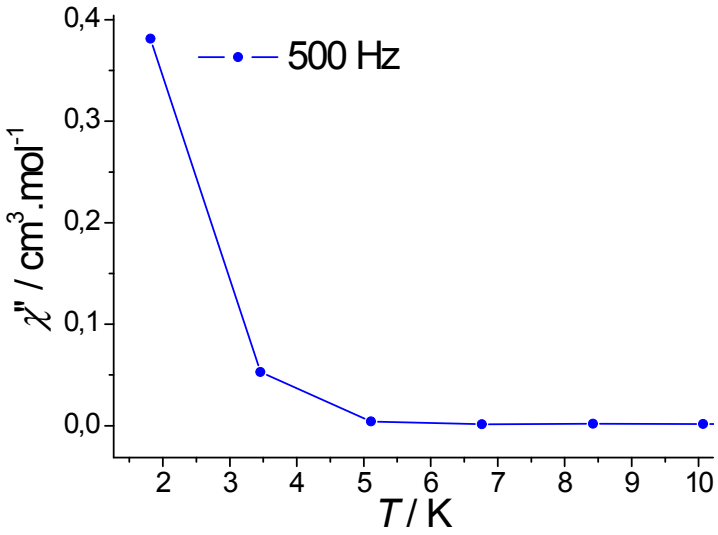

Figure S18. Temperature dependence of the out-of-phase susceptibility, χ'', under a 2500 DC field for **3**.

Table S1. Crystallographic data and structural refinement details for **1**–**3.**

	1a	**1b**	**2**	**3**
Empirical formula	$C_{65.89}H_{106.71}DyLiN_4O_{6.94}$	$C_{68.5}H_{112.5}DyLiN_4O_6$	$C_{69}H_{114}LiN_4O_7Tb$	$C_{67}H_{109}ErLiN_4O_6$
Formula weight	1235.40	1257.56	1277.50	1240.78
Crystal system	Orthorhombic	Monoclinic	Monoclinic	Monoclinic
Space group	$P2_12_12_1$	$P2_1/c$	$P2_1/c$	$P2_1/c$
a, Å	16.12320(10)	17.9746(9)	18.126(3)	16.8819(19)
b, Å	17.39480(10)	15.7488(8)	15.536(3)	15.9384(13)
c, Å	24.3737(2)	26.9666(14)	26.498(5)	27.699(2)
α, °	90	90	90	90
β, °	90	107.7100(10)	107.529(3)	103.719(9)
γ, °	90	90	90	90
Volume, Å^3	6835.84(8)	7271.9(6)	7115(2)	7240.4(12)
Z	4	4	4	4
ρ_{calc}, Mg/m^3	1.200	1.149	1.193	1.138
Absorption coeff., mm^{-1}	1.143	1.074	1.044	1.205
F(000)	2618	2674	2720	2632
Crystal size, mm	0.50×0.50×0.40	0.37×0.23×0.15	0.42×0.18×0.16	0.35×0.20×0.07
θ range for data collection, °	3.03–30.00	2.38–27.00	2.36–25.03	2.86–25.00
Index range	$-22 \le h \le 22$ $-24 \le k \le 24$ $-34 \le l \le 34$	$-22 \le h \le 22$ $-20 \le k \le 20$ $-34 \le l \le 34$	$-21 \le h \le 21$ $-18 \le k \le 18$ $-31 \le l \le 31$	$-19 \le h \le 20$ $-18 \le k \le 18$ $-32 \le l \le 32$
Reflections collected	159230	78191	58095	59623
Independent reflections	19899	15758	12571	12657
R_{int}	0.041	0.0389	0.0815	0.1073
Completeness to θ, %	99.7	99.1	99.9	99.3
GooF	1.105	1.047	1.171	1.030
R_1 ($I > 2\sigma(I)$)	0.0397	0.0338	0.0883	0.0575
R_2 (all data)	0.1006	0.0893	0.2360	0.1463
Largest diff. peak and hole, e/Å^3	1.578 / -1.210	1.630 / -0.855	1.580 / -3.226	2.044 / -0.701

Table S2. Bond lengths, angles and SHAPE analysis in **1**–**3.**

	Ln-N (Å)	Ln-C	Centroids-Ln-Centroids angle (°)
1a	2.221(3)-2.256(3)	2.672(4)-2.698(4)	172.2
1b	2.229(2)-2.254(2)	2.673(2)-2.711(2)	169.5
2	2.205(7)-2.256(6)	2.652(8)-2.700(8)	170.0
3	2.211(5)-2.244(4)	2.653(6)-2.702(6)	171.5

	SP	T	SS
1a	21.040	6.075	6.159
1b	19.644	6.273	6.404
2	21.008	6.111	6.591
3	22.031	5.079	6.346

SP: Square Planar
T: Tetrahedron
SS: Seesaw

Table S3. Fitting of the Cole-Cole plots with a generalized Debye model for temperature ranging from 1.8 to 22 K under a zero DC field for **1a**.

T (K)	α	χ_S (cm^3. mol^{-1})	χ_T (cm^3. mol^{-1})
1.80	0.260	1.344	5.422
2.50	0.224	1.019	3.995
3.00	0.243	0.881	3.347
5.00	0.204	0.553	2.079
7.00	0.179	0.403	1.518
8.00	0.161	0.357	1.342
9.27	0.146	0.302	1.168
10.54	0.117	0.267	1.041
11.81	0.102	0.236	0.936
13.09	0.182	0.169	0.796
14.36	0.0466	0.197	0.789
15.63	0.0647	0.188	0.722
16.91	0.074	0.163	0.667

19.19	0.0669	0.155	0.623
19.45	0.128	0.136	0.571
20	0.005	0.215	0.581
22	0.0517	0.154	0.522

Table S4. Energies of the lowest Kramers doublets (cm^{-1}) of Dy center.

Spin-orbit energies, cm^{-1}		**Angles between the magnetic axes of the lowest and excited KDs, (°)**
Dy_basis1	**Dy_basis2**	
0.000 245.236 438.266 501.062 584.614 634.508 780.481 895.575	0.000 236.453 410.703 444.167 552.230 614.478 750.834 894.952	- 8.60842 58.602 54.802 50.2658 91.4544 59.282 89.7924

Table S5. The *g* tensors of the two lowest Kramers doublets (KD) of Dy center.

KD		Dy_**basis1**	Dy_**basis2**
		g	***g***
1	g_X	0.002383	0.004320
	g_Y	0.006008	0.007958
	g_Z	19.724867	19.707419
2	g_X	0.124545	0.095208
	g_Y	0.130856	0.101489

	g_Z	16.719800	16.690874
3	g_X	0.861059	0.307556
	g_Y	0.883754	0.725234
	g_Z	13.321508	14.425136
4	g_X	0.6289345	0.702353
	g_Y	1.144515	2.055076
	g_Z	17.371102	12.802994

Table S6. Fitting of the Cole-Cole plots with a generalized Debye model for temperature ranging from 1.8 to 22 K under a 3500 Oe DC field for **1a**.

T (K)	α	χ_S (cm^3. mol^{-1})	χ_T (cm^3. mol^{-1})
3.84	0.143	0.426	1.774
6.00	0.163	0.376	1.638
7.95	0.229	0.302	1.303
10.00	0.205	0.237	1.053
12.00	0.189	0.197	0.885
13.79	0.196	0.180	0.779
15.59	0.162	0.161	0.698
17.40	0.125	0.155	0.639
19.19	0.164	0.150	0.573
21.00	0.071	0.152	0.542
21.50	0.094	0.152	0.526
22.15	0.103	0.156	0.509

Table S7. Fit parameters obtained using the equation $\tau^{-1} = \tau_0^{-1}\exp(-\Delta/kT) + CT^n + AT^n + \tau^{-1}_{QTM}$

Compound	Δ_{orbach} (cm^{-1})*	τ_0 (s)*	Δ (cm^{-1})	τ_0 (s)	A (s^{-1}.K^{-1})	C(s^{-1}.K^{-9})	C(s^{-1}.K^{-7})	τ_{QTM} (s)
1a (0 Oe)	43 ± 5	(6.6 ± 0.3) × 10^{-6}	30 ± 2	(3.1 ± 0.5) × 10^{-6}	-	(3.0 ± 0.2) × 10^{-9}	-	(1.22 ± 0.06) × 10^{-3}
1a (3500 Oe)	108 ± 5	(2.0 ± 0.3) × 10^{-7}	35 ± 5	(8 ± 3) × 10^{-5}	0 ± 4	(2.31 ± 0.08) × 10^{-11}	-	-
1b (0 Oe)	49 ± 6	(4.9 ± 0.3) × 10^{-6}	21 ± 2	(9 ± 1) × 10^{-5}	-	(5.5 ± 0.2) × 10^{-9}		(1.35 ± 0.07) × 10^{-3}
2 (900 Oe)	21 ± 1	(6.4 ± 0.2) × 10^{-6}	17 ± 1	(2.0 ± 0.3) × 10^{-5}	100 ± 10	-	(1.8 ± 0.2) × 10^{-4}	-

*****obtained from the linear fit using the high-temperature region*

Table S8. Energies of the lowest doublets (cm^{-1}) of Tb center.

Spin-orbit energies, cm^{-1}		Angles between the magnetic axes of the lowest and excited KDs, (°)
Tb_basis1	**Tb_basis2**	
0.000	0.000	-
0.034	0.023	
227.680	257.182	45.4897
228.332	257.319	
323.263	336.396	42.5286
324.069	339.835	
471.097	481.968	44.4467
475.334	495.914	
560.293	573.848	43.5371
669.515	678.059	43.2284
697.717	710.134	
757.009	749.984	60.6391
765.777	762.084	

Table S9. The *g* tensors of the two lowest doublets (KD) of Tb center.

D		Tb_**basis1** ***g***	Tb_**basis2** ***g***
1	g_X g_Y g_Z	0 0 17.887156	0 0 17.896861
2	g_X g_Y g_Z	0 0 15.808805	0 0 15.536348
3	g_X g_Y g_Z	0 0 11.976033	0 0 11.877624
4	g_X g_Y g_Z	0 0 9.073788	0 0 9.358402

Table S10. Fit parameters of the field dependence of the relaxation time obtained using the Eq. 2 for **2** and **4.**

Compound	*D* ($s^{-1}K^{-1}Oe^{-2}$)	B_1 (s^{-1})	B_2 (Oe^{-2})	*K*
2	1.762×10^{-5}	541.28	9.52×10^{-6}	44.89

Table S11. Fit parameters of the field dependence of the relaxation time obtained using the Eq. 3 for **2**.

Compound	Δ_{Orbach} (cm^{-1})	τ_0 (s)	*C* ($s^{-1}.K^{-9}$)	*C* ($s^{-1}.K^{-7}$)	*D* ($s^{-1}K^{-1}Oe^{2}$)*	B_1 (s^{-1})*	B_2 (Oe^{-2})*
2 (900 Oe)	12.2 ± 0.5	3.77×10^{-5}	-	2.429×10^{-4}	1.762×10^{-5}	541.28	9.52×10^{-6}

Table S12. Fitting of the Cole-Cole plots with a generalized Debye model for temperature ranging from 1.8 to 10.25K under a 900 Oe DC field for **2**.

T (K)	α	χ_S ($cm^3.\ mol^{-1}$)	χ_T ($cm^3.\ mol^{-1}$)
1.80	0.235	1.308	4.10714
2.00	0.220	1.188	3.759
2.25	0.216	1.080	3.409
2.50	0.226	1.000	3.085
2.75	0.190	0.910	2.895
3.00	0.203	0.857	2.663
3.25	0.156	0.791	2.507
3.50	0.162	0.746	2.354
3.75	0.149	0.702	2.227
4.00	0.322	0.757	2.004
4.25	0.143	0.627	1.989
4.50	0.038	0.617	1.945
4.75	0.112	0.582	1.808
5.00	0.104	0.559	1.728
5.25	0.100	0.540	1.653
5.50	0.093	0.521	1.586
5.75	0.087	0.505	1.524
6.00	0.006	0.491	1.501
6.25	0.080	0.477	1.413

6.50	0.065	0.464	1.369
6.75	0.064	0.453	1.321
7.00	0.061	0.443	1.278
7.25	0.138	0.418	1.208
7.50	0.057	0.423	1.200
7.75	0.053	0.416	1.164
8.00	0.020	0.440	1.142
8.25	0.055	0.397	1.097
8.50	0.057	0.389	1.066
8.75	0.085	0.368	1.029
9.00	0.039	0.382	1.012
9.25	0.0004	0.392	0.990
9.50	0.018	0.381	0.968
9.75	0.005	0.384	0.949
10.00	0.023	0.366	0.922
10.25	0.0004	0.381	0.906

Table S13. Energies of the lowest Kramers doublets (cm^{-1}) of Er center.

Spin-orbit energies, cm^{-1}		**Angles between the magnetic axes of the lowest and excited KDs, (°)**
Er_basis1	**Er_basis2**	
0.000	0.000	-
22.544	27.694	8.49177
62.719	82.869	
111.773	113.070	82.5903
214.127	226.835	

287.078 446.157	301.041 439.586	86.0442 84.6532 89.6718 86.9124 86.4033

Table S14. The *g* tensors of the two lowest Kramers doublets (KD) of Er center.

KD		Er_**basis1** ***g***	Er_**basis2** ***g***
1	g_X g_Y g_Z	1.317902 5.785255 12.442243	1.206265 6.205133 12.078836
2	g_X g_Y g_Z	8.317705 5.002762 1.045869	1.256502 4.672803 8.520682
3	g_X g_Y g_Z	0.080384 3.475915 13.180474	1.504798 3.529860 13.384534
4	g_X g_Y g_Z	4.658639 4.751195 8.714168	3.616702 4.581772 8.822376

1 M. Svoboda and H. t. Dieck, *Journal of Organometallic Chemistry*, 1980, **191**, 321.
2 M. D. Taylor and C. P. Carter, *Journal of Inorganic and Nuclear Chemistry*, 1962, **24**, 387.
3 S. J. Lyle and M. M. Rahman, *Talanta*, 1963, **10**, 1177.
4 G. Sheldrick, *Acta Cryst. A*, 2015, **71**, 3.
5 G. Sheldrick, *Acta Cryst. C*, 2015, **71**, 3.
6 Agilent, *CrysAlis PRO*, 2014, Agilent Technologies Ltd, Yartnon, Oxfordshire, England.
7 Bruker, *SADABS*, 2001, Bruker AXS Inc., Madison, Wisconsin, USA.
8 J. M. Zadrozny, M. Atanasov, A. M. Bryan, C.-Y. Lin, B. D. Rekken, P. P. Power, F. Neese and J. R. Long, *Chem. Sci.*, 2013, **4**, 125.
9 P. L. Scott and C. D. Jeffries, *Phys. Rev.*, 1962, **127**, 32.
10 N. F. Chilton, D. Collison, E. J. L. McInnes, R. E. P. Winpenny and A. Soncini, *Nat. Commun.*, 2013, **4**.